A simplified modelling strategy for R/C walls satisfying PS92 and EC8 design

Panagiotis Kotronis, F. Ragueneau, J. Mazars

A simplified modelling strategy for R/C walls satisfying PS92 and EC8 design

Panagiotis Kotronis[a,*], Frédéric Ragueneau[b], Jacky Mazars[a]

[a] *Laboratoire Sols, Solides, Structures (3S), Domaine Universitaire BP 53, 38041 Grenoble cedex 9, France*
[b] *Laboratoire de Mécanique et de Technologie (LMT), 61 av. du Prés. Wilson, 94235 Cachan cedex, France*

According to the French code PS92 lightly reinforced concrete walls subjected to earthquake ground motion are designed following the "multifuse" concept. Low percentages of reinforcement combined with an appropriate distribution at several levels lead to dissipation of energy via wide crack patterns at different heights of the wall. On the contrary, design according to Eurocode 8 (EC8) privileges dissipation at a single flexural plastic hinge at the base. The rest of the wall is over-designed in flexure to avoid development of plastic behaviour anywhere above the base region ("monofuse" concept). A simplified modelling strategy based on the principles of damage mechanics, plasticity and classical Bernoulli beam theory is used to simulate the 2D non-linear behaviour of two mock-ups satisfying the above design provisions. CAMUS I and III specimens have the same geometry and follow PS92 and EC8 design philosophies respectively. Comparison with the experimental results, obtained on a shaking table, gives an insight into the behaviour of the structures and shows the ability but also the limitations of the approach.

Keywords: Concrete; Wall; Damage; Shaking table; EC8; Beam

1. Introduction

Simulating the non-linear behaviour of reinforced concrete (R/C) walls subjected to severe earthquake ground motion is an important problem for the engineering community. Non-linear dynamic analysis based on a detailed finite element model requires large-scale computations and delicate solution techniques. The necessity to perform parametric studies and the stochastic nature of the input accelerations often impose simplified numerical modelling that reduces computational cost. Nevertheless, in order to describe efficiently the non-linear time history behaviour it is necessary to have:

1. A realistic model to describe the materials;
2. An optimum idealization i.e. one that is sufficiently fine and yet not too costly;
3. An accurate description of boundary conditions.

The classical Bernoulli beam theory is used to describe the non-linear behaviour of R/C walls. 2D beams are divided in several layers where simple uni-axial constitutive relationships are used, sufficiently general though to take into account all the different inelastic phenomena (cracking by damage, irreversible deformation by plasticity and crack-closing by unilateral frictional contact condition). The proposed modelling strategy is used to simulate the non-linear behaviour of two specimens tested on the Azalée shaking table of the EMSI Laboratory at CEA Saclay (the largest shaking table in Europe). CAMUS I and III mock-ups have the same geometry and were designed following the French code PS92 [1] and the Eurocode 8 [2] respectively.

The paper begins with the tools used for a simplified dynamic analysis and the constitutive laws for concrete and steel. Presentation of the tests at CEA Saclay and

* Corresponding author. Tel.: +33 (0)4 76 82 51 75; fax: +33 (0)4 76 82 70 00.
E-mail address: Panagiotis.Kotronis@inpg.fr (P. Kotronis).

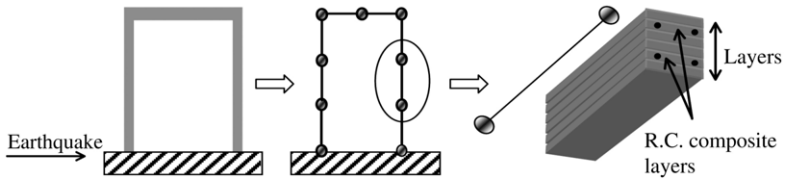

Fig. 1. Multi-layered beam discretization for R/C structures.

description of the two specimens follow. Emphasis is put on the differences of the mock-ups and the code design philosophies. The numerical model used for the simulation of the specimens is presented in detail. Finally, verification of the proposed modelling strategy is provided through comparison of the numerical with the experimental results and a discussion is made on the different types of failure of the mock-ups and the influence of the local numerical variables on global quantities.

2. Tools for a simplified dynamic analysis of R/C structures

2.1. Spatial and time discretization

In order to limit the complexity of the model and the resulting computational costs structures are simulated using multi-layered Bernoulli beam elements and concentrated masses at specific points ([3,4] – this approach is the 2D version of the classical multifibre beam element [5–9]). 1D constitutive laws are attributed at each layer and the seismic loading is applied as an input motion at the base (Fig. 1).

Dynamic analysis for earthquake ground motion reduces to solving the following set of non-linear equations [10]:

$$\mathbf{M}\ddot{u}(t) + \mathbf{C}\dot{u}(t) + f^{\text{int}}(u,t) = -\mathbf{M}\ddot{u}_g(t) \tag{1}$$

where $\mathbf{M}$ and $\mathbf{C}$ are, respectively, mass and damping matrix, $\ddot{u}(t)$ and $\dot{u}(t)$ are nodal accelerations and velocities, $f^{\text{int}}(u,t)$ is the internal force vector and $\ddot{u}_g(t)$ is the ground acceleration applied on the structure. By using a time-integration scheme, the differential equation of motion in (1) is reduced to an algebraic equation. In particular, for low frequency response in earthquake engineering analysis one uses an implicit scheme such as the Newmark one-step scheme (where $\gamma = 1/2$ and $\beta = 1/4$ – the constants for Newmark's time-integration scheme – are typically chosen for optimal result accuracy [11]). The discrete set of equations obtained is further solved by an iterative solution procedure, where the secant stiffness matrix $\mathbf{K}$ is used instead of an updated one (quasi-Newton method), as is usually the case for damage constitutive laws [12].

Remarks. 1. For the cases where shear deformations become important the Bernoulli hypothesis – sections remain plain and perpendicular to the neutral axis of the beam – is not valid and one has to use Timoshenko multi-layered (multifibre) beams [5,8,9,13].

2. When dealing with structures with a slenderness ratio far from the classical beam theory a more reliable representation of shear deformations and shear stresses has to be provided. One possibility in that respect – always within the family of simplified modelling strategies – is to use the Equivalent Reinforced Concrete model that privileges the use of lattice meshes for concrete and reinforcement bars [14,15].

2.2. Modelling the damping mechanism

In the case of mode superposition techniques, the dynamic response of the system is the sum of stationary waves. The problem to solve consists of the computation of the eigenfrequencies, the corresponding mode-shapes and their relative contribution to the global response. Considering the superposition of harmonic functions, the solution breaks down to the following eigenvalue problem [10,16]:

$$|\mathbf{K} - \omega_i^2 \mathbf{M}| = 0 \tag{2}$$

where ω_i is the natural frequency of vibration for the mode i.

A viscous Rayleigh-type matrix for damping (linear combination of the mass and damping matrices) does not create identical levels of dissipation depending on the way the equation of motion is expressed. Indeed, a simple analysis on a single degree of freedom structure allows pointing out the discordance with regard to the dissipated energy between a description of the motion in the relative or in the absolute reference frame [17,18]. If a stiffness matrix is 'insensitive' to the rigid body motion, the contribution of the mass matrix generates spurious dissipation. In order to avoid the drawbacks of a viscous Rayleigh damping matrix in the presence of rigid body motion for finite element codes where the equation of motion is treated in the absolute reference frame, the damping for each mode i depends only on the modal stiffness introducing no contribution of the mass [17]. This damping matrix is a non-diagonal one (non-classical damping). This feature may become a major drawback in the case of structures with a lot of degrees of freedom. Nevertheless, for simplified analysis the number of degrees of freedom remains relatively small.

2.3. Materials constitutive relations

Both steel and concrete are described within the thermodynamic framework for irreversible processes [19]. In

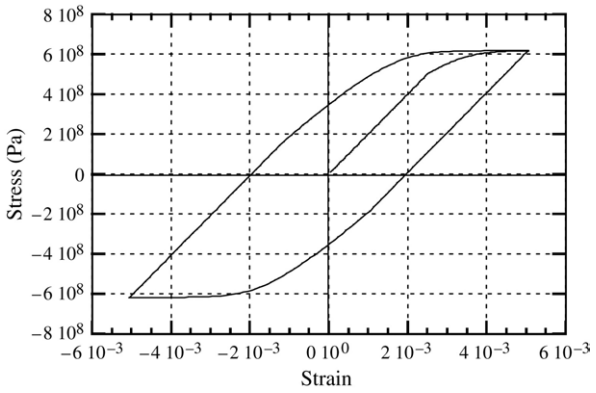

Fig. 2. Uni-axial response of steel model for cyclic loading.

order to describe the non-linear behaviour of reinforcement bars, we choose a classical plasticity model taking into account the non-linear kinematic hardening of Armstrong and Frederick [20]. The free energy density for this model $\rho\psi$ can be written as:

$$\rho\psi = \frac{1}{2}(\boldsymbol{\varepsilon} - \boldsymbol{\varepsilon}_{\mathbf{p}}) : \mathbf{H} : (\boldsymbol{\varepsilon} - \boldsymbol{\varepsilon}_{\mathbf{p}}) + \frac{1}{2} b\boldsymbol{\alpha} : \boldsymbol{\alpha} \tag{3}$$

where $\mathbf{H}$ is the Hooke's elasticity tensor, $\boldsymbol{\varepsilon}_{\mathbf{p}}$ is the plastic strain tensor, $\boldsymbol{\varepsilon}$ the strain tensor, $\boldsymbol{\alpha}$ a tensorial internal variable associated with the kinematic hardening and b a material parameter. The constitutive equations for this kind of model are derived as follows:

$$\boldsymbol{\sigma} = \frac{\partial(\rho\psi)}{\partial\boldsymbol{\varepsilon}} = \mathbf{H} : (\boldsymbol{\varepsilon} - \boldsymbol{\varepsilon}_{\mathbf{p}}) \tag{4}$$

$$\mathbf{X} = \frac{\partial(\rho\psi)}{\partial\boldsymbol{\alpha}} = b\boldsymbol{\alpha} \tag{5}$$

where $\boldsymbol{\sigma}$ is the stress tensor and $\mathbf{X}$ is the back-stress hardening variable. The latter is used to describe a modified form of the plasticity criterion allowing us to remain within the associated plasticity framework:

$$f = J_2(\boldsymbol{\sigma} - \mathbf{X}) + \frac{3}{4} a\mathbf{X} : \mathbf{X} - \sigma_y \leq 0 \tag{6}$$

where a and σ_y are material parameters and J_2 the second invariant of the deviatoric stress tensor.

Due to the particular geometric characteristics of steel bars, only a 1D implementation of the model is carried out. Reinforcement bars are introduced within special composite layers (see Fig. 1), whose behaviour is obtained as a combination of those of concrete and steel according to:

$$\sigma_{\text{layer}} = (1 - \alpha_{\text{rel}})\sigma_{\text{concrete}} + \alpha_{\text{rel}}\sigma_{\text{steel}} \tag{7}$$

where σ_{layer} denotes axial stresses in the layer, σ_{concrete} and σ_{steel} axial stresses in the concrete and the steel respectively in the layer and α_{rel} is the relative area of the reinforcement in the layer. A typical stress–strain cyclic response predicted by this model is given in Fig. 2.

The constitutive models able to reproduce realistically the non-linear behaviour of concrete are often based on damage mechanics (e.g. [12,21–24]), on plasticity theory (e.g. [25,26]) or using the microplane concept (e.g. [27–29]). The constitutive model for concrete used in this work is based on damage mechanics and takes into account some observed phenomena under cyclic loading such as decrease in material stiffness due to cracking, stiffness recovery (damage deactivation) which occurs at crack closure and inelastic strains concomitant to damage [30]. It has two scalar damage variables, D_1 for damage in tension and D_2 for damage in compression. The Gibbs free energy χ of this model in its 3D formulation can be expressed as:

$$\chi = \frac{\langle\boldsymbol{\sigma}\rangle_+ : \langle\boldsymbol{\sigma}\rangle_+}{2E(1-D_1)} + \frac{\langle\boldsymbol{\sigma}\rangle_- : \langle\boldsymbol{\sigma}\rangle_-}{2E(1-D_2)} + \frac{\nu}{E}(\boldsymbol{\sigma} : \boldsymbol{\sigma} - \text{Tr}(\boldsymbol{\sigma}^2)) + \frac{\beta_1 D_1}{E(1-D_1)} f(\boldsymbol{\sigma}) + \frac{\beta_2 D_2}{E(1-D_2)}\text{Tr}(\boldsymbol{\sigma}) \tag{8}$$

$f(\boldsymbol{\sigma})$ is the crack closure function. $\langle\cdot\rangle_+$ denotes the positive part of a tensor. E is the initial Young's modulus and ν the Poisson ratio. β_1 and β_2 are material constants and $\text{Tr}(\boldsymbol{\sigma}) = \sigma_{ij}\delta_{ij}$. The total strain is:

$$\boldsymbol{\varepsilon} = \boldsymbol{\varepsilon}^{\mathbf{e}} + \boldsymbol{\varepsilon}^{\mathbf{in}} \tag{9}$$

$$\boldsymbol{\varepsilon}^{\mathbf{e}} = \frac{\langle\boldsymbol{\sigma}\rangle_+}{E(1-D_1)} + \frac{\langle\boldsymbol{\sigma}\rangle_-}{E(1-D_2)} + \frac{\nu}{E}(\boldsymbol{\sigma} - \text{Tr}(\boldsymbol{\sigma})\mathbf{1}) \tag{10}$$

$$\boldsymbol{\varepsilon}^{\mathbf{in}} = \frac{\beta_1 D_1}{E(1-D_1)}\frac{\partial f(\boldsymbol{\sigma})}{\partial\boldsymbol{\sigma}} + \frac{\beta_2 D_2}{E(1-D_2)}\mathbf{1} \tag{11}$$

with $\boldsymbol{\varepsilon}^{\mathbf{e}}$ elastic strains, $\boldsymbol{\varepsilon}^{\mathbf{in}}$ inelastic strains and $\mathbf{1}$ denotes the unit tensor.

Damage criteria are expressed as $f_i = Y_i - Z_i$ ($i = 1$ for tension or 2 for compression, Y_i is the associated force to the damage variable D_i and Z_i a threshold dependent on the hardening variables). The evolution laws for the damage variables D_i are finally written as

$$D_i = 1 - \frac{1}{1 + [A_i(Y_i - Y_{0i})]^{B_i}}. \tag{12}$$

The crack closure function is defined as follows,

$$\begin{cases} \text{Tr}(\boldsymbol{\sigma}) \in [0, +\infty) \rightarrow \dfrac{\partial f(\boldsymbol{\sigma})}{\partial\boldsymbol{\sigma}} = \mathbf{1} \\ \text{Tr}(\boldsymbol{\sigma}) \in [-\sigma_f, 0) \rightarrow \dfrac{\partial f(\boldsymbol{\sigma})}{\partial\boldsymbol{\sigma}} = \left(1 - \dfrac{\text{Tr}(\boldsymbol{\sigma})}{\sigma_f}\right)\mathbf{1} \\ \text{Tr}(\boldsymbol{\sigma}) \in (-\infty, -\sigma_f) \rightarrow \dfrac{\partial f(\boldsymbol{\sigma})}{\partial\boldsymbol{\sigma}} = 0.\mathbf{1} \end{cases} \tag{13}$$

Y_{0i} is the initial elastic threshold ($Y_{0i} = Z_i(D_i = 0)$), σ_f the crack closure stress and A, B material constants. Due to the spatial discretization with 2D multi-layered Bernoulli beam elements only a 1D implementation of the model is carried out (shear is considered linear). Fig. 3 gives the stress–strain response of the model for a uni-axial traction–compression loading.

3. Shaking table tests

This section presents a summary of the CAMUS I and III shaking table tests. The design of the specimens corresponds to the same level of design lateral forces (CAMUS III has

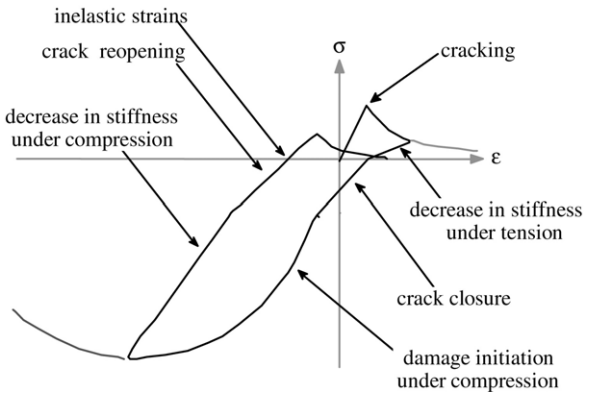

Fig. 3. Uni-axial response of concrete model for cyclic loading.

the same target flexural capacity at the base as CAMUS I, namely $M_{Sd} = 390$ kN m). The design of CAMUS I follows PS92 provisions, where the choice of reinforcement is made so that cracking spreads as much as possible through the structure. On the contrary, CAMUS III adopts EC8 philosophy that prefers dissipation at a single flexural plastic hinge at the base. The rest of the wall is over-designed in flexure, to avoid development of plastic behaviour anywhere above the base region. Dynamic tests have been performed until collapse of the structures on the Azalée shaking table of the EMSI Laboratory at CEA Saclay. By collapse we mean the appearance of significant cracks on the concrete walls and important plastic strain with possible failure of some bars of the vertical reinforcing steel. A detailed presentation covering all aspects of the experimental programs can be found in [31,32].

Remarks. 1. In order to compare and validate the numerical tools commonly used for R/C load bearing walls, international benchmarks have been organized around the CAMUS I and III experiments [33–36].
2. The CAMUS III experiment is part of the 5th Topic "Shear Wall Structures" of the European program ICONS-TMR ("Innovative Seismic Design Concepts for New and Existing Structures – Training and Mobility of Researchers") and of ECOEST2 ("European Consortium of Earthquake Shaking Tables") – see [37] for the final report.

3.1. Geometrical characteristics of the specimens

The overall geometry of CAMUS I and III is the same. The 1/3 scaled models are composed of two parallel five-floor R/C walls without opening linked by six square floors. They have a total height of 5.1 m. A highly reinforced footing allows the anchorage to the shaking table (Fig. 4).

The walls are loaded in their own plane. Stiffness and strength in the perpendicular direction are increased by adding triangular bracing so as to reduce the risk of possible failure due to some parasite transversal motion of a non-symmetric failure of the structural walls.

3.2. Mass description

The total mass of each specimen is estimated at about 36 000 kg. The mass of each floor, without the additional masses, is about 1300 kg. The additional masses were determined in order to impose a normal force to the walls compatible with the vertical stress values commonly found at the base of such structures – 1.6 MPa in this case (see Fig. 4).

3.3. Concrete and steel reinforcement

Typical concrete mixtures were used for the casting of the mock-ups. Their characteristics were checked by the usual compressive and splitting tests.

The design of CAMUS I and III is meant to correspond to the same level of design lateral forces and ultimate bending moment at the base. This flexural capacity is used to define the amount of vertical reinforcement at the base (the same for both specimens). The difference in reinforcement is significant for the upper levels according to Fig. 4 and Table 1: the French design code PS92 allows yielding at several heights of the specimen while EC8 concentrates dissipation at the base (capacity design philosophy). For CAMUS III the amount of vertical reinforcement above the base aims to provide the flexural over strength required by EC8 (Table 1). Tensile tests performed before the tests helped to define the properties of the steel bars.

Table 1
Steel reinforcement for each wall (mm^2)

	CAMUS I		CAMUS III	
	Sa, Sb	Sc	Sa, Sb	Sc
Level 5	15.9	78.4	132.4	159
Level 4	28.3	78.4	233	159
Level 3	94.4	110.2	233	159
Level 2	188.9	138	289.6	159
Level 1	289.4	138	289.6	159

(Sa, Sb and Sc see Fig. 4).

3.4. Loading conditions

Since the mock-ups were loaded with horizontal acceleration signals parallel to the walls and the steel bracing systems at each floor level prevented occurrence of any torsion mode the problem is a two-dimensional one. Three types of ground motion are imposed: The artificial Nice S1 signal, representative of a far field earthquake and of the French design acceleration spectra, the San Francisco and Melendy Ranch signals representative of near field earthquakes. The complete experimental sequence was different for the two specimens (Table 2).

The three ground motions and their spectra (5% damping) are presented in Figs. 5 and 6. Nice S1 is rich in terms

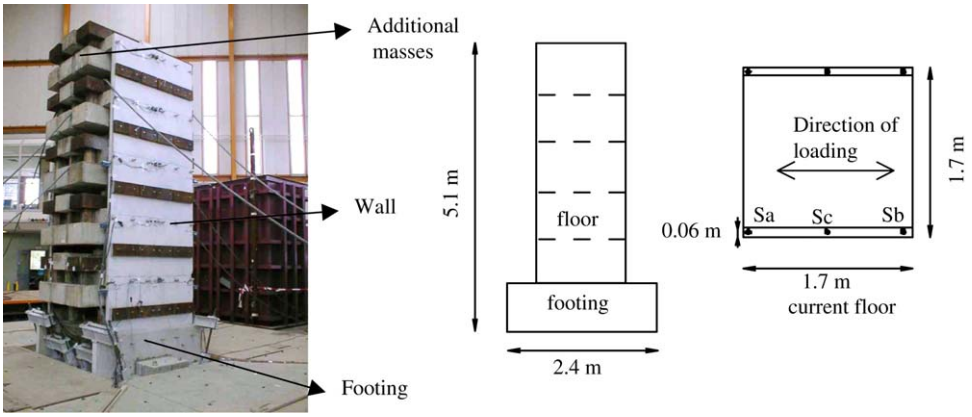

Fig. 4. Geometrical characteristics of the CAMUS I and CAMUS III specimens.

Table 2
Experimental sequences

CAMUS I	CAMUS III
Nice S1 0.24*g*	Nice S1 0.42*g*
San Francisco 1.13*g*	Nice S1 0.24*g*
Nice S1 0.40*g*	Melendy Ranch 1.35*g*
Nice S1 0.71*g*	Nice S1 0.64*g*
–	Nice S1 1.00*g*

of frequencies. San Francisco and Melendy Ranch are short; they have a thinner effective bandwidth of higher accelerations. The frequency content of the Melendy Ranch signal is rich around 7 Hz, which was proven to be approximately the first natural frequency of the CAMUS III specimen (6.88 Hz).

4. Numerical simulations

4.1. Numerical model

The 2D numerical model represents each wall as a cantilever beam whose behaviour is controlled primarily by bending. Each wall is divided into 24 Bernoulli beam elements with 37 layers each. Concentrated masses are introduced at each floor. A single wall is considered (Fig. 7).

For the first numerical simulations of the CAMUS I specimen the model was supposed fixed to the shaking table. The first natural frequency of the specimen predicted by this model was however different from the real one measured before the test using a low level white noise (10.3 Hz for the model instead of 7.3 Hz for the measured one). The model failed also to reproduce the second frequency representative of the pumping–axial deformation mode – (40 Hz instead of 20 Hz). Thus, it was necessary to take into account the influence of the shaking table and the anchorage system. A simple modelling of the basement boundary conditions is achieved by the use of a horizontal bending beam (Fig. 7). Knowing the measured shaking table stiffness helped to adjust the vertical ($K_v = 48EI/l^3$) as well as the rotational stiffness ($K_\theta = 12EI/l$) of the boundary element so as to better approximate the first two modes (see Table 3) – I being the moment of inertia and l the length of the boundary element. The same stiffness – without further adjustments – is used for the CAMUS III mock-up, making for this case the comparison with the experimental results similar to the one of a "blind simulation" in order for the reader to test the efficiency of the model.

Table 3
Adjusting the numerical model for the CAMUS I specimen

	Initial modelling (Hz)	Adjusted modelling (Hz)	Measured frequencies (Hz)
1*st mode*	10.3	7.4	7.3
2*nd mode*	40.0	19.0	20.0

Constitutive laws for concrete and steel are used in 1D formulation. Specific values for the materials are chosen according to compressive, tensile and splitting tests (Table 4). More specifically, for the damage model one has: $A_1 = 9.0\text{E}{+}03$ MPa^{-1}, $A_2 = 5.3$ MPa^{-1}, $B_1 = 1.2$, $B_2 = 1.4$, $\beta_1 = 1.0$ MPa, $\beta_2 = -40$ MPa, $Y_{01} = 2.2\text{E}{-}04$ MPa, $Y_{02} = 0.9\text{E}{-}02$ MPa, $\sigma_f = 1.3$ MPa. The Young's modulus of the base slab is taken smaller due to localized cracking already visible before the tests (those cracks appeared during the assembly of the specimens on the table particularly during the tightening of the wall anchorage to the floors). Bond slip and confinement are not taken into account. The damping coefficients have been adjusted to ensure a value of 2% on the two first modes.

The motions are applied to the specimens according to the sequences presented in Table 2 so as to accumulate damage and not one by one on a virgin model. Results are compared in terms of global and local quantities (time history of displacements and forces, variation of axial force, steel strain, damage distribution).

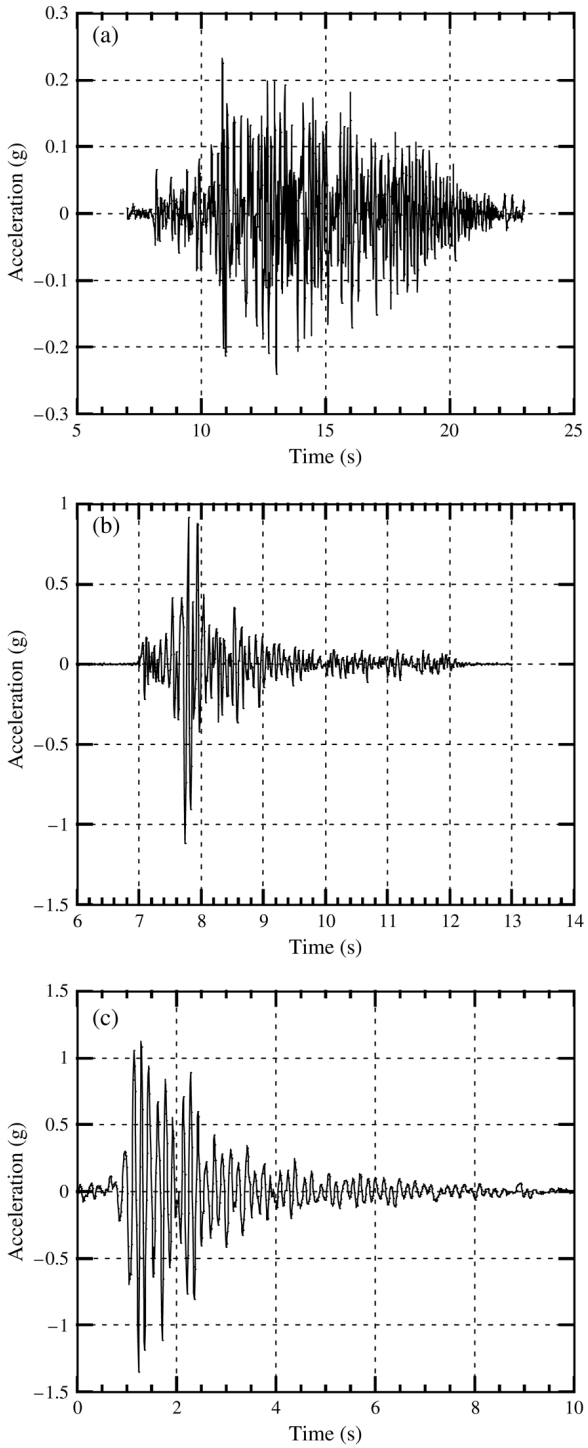

Fig. 5. Ground motions: (a) Nice ($a_{max} = 0.25g$), (b) San Francisco ($a_{max} = 1.11g$) and (c) Melendy Ranch ($a_{max} = 1.35g$).

4.2. Time history of displacements and forces

For the CAMUS I mock-up, at initial level when concrete starts cracking in tension and the reinforcement bars reach the yield stress, the global behaviour of the structure is well represented by the numerical model. The loss in stiffness during the later stages of loading and the decrease of

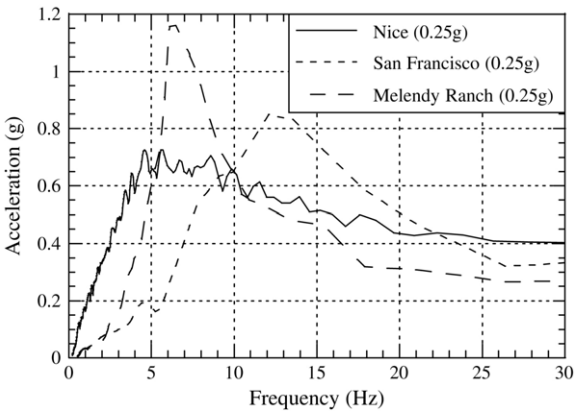

Fig. 6. Response spectra (5% damping).

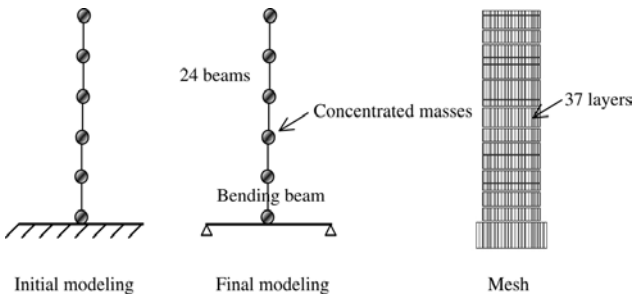

Fig. 7. 2D numerical model for the CAMUS I and III specimens.

Table 4
Specific values used for the materials

		CAMUS I	CAMUS III
Compression strength (concrete)	MPa	35	30
Tensile strength (concrete)	MPa	3	2.5
Young's modulus (concrete)	MPa	30 000	30 000
Young's modulus at the base (concrete)	MPa	15 000	15 000
Poisson coefficient (concrete)	–	0.2	0.2
Yield stress (steel)	MPa	414	414
Young's modulus (steel)	MPa	200 000	200 000

the fundamental frequency is also predicted in a fairly acceptable manner, with the maximum displacement always remaining slightly underestimated before and overestimated after the maximum loading level is reached (Figs. 8 and 9). Displacement is measured at the top of the wall. Table 5 summarizes comparisons of experimental and computed results for the reaction forces and indicates globally a very good agreement.

The modal analysis of the CAMUS III specimen shows that the numerical model is stiffer than the mock-up (Table 6). Due to an unreliable displacement transducer at the top of the specimen comparison of displacements is presented only at the fifth floor. During the first two sequences CAMUS III stays practically in the elastic zone without yielding of the steel bars. Simulation predicts

Table 5
CAMUS I – global response comparisons

	Displacement (cm)		Shear force (kN)		Moment (kN m)		Axial force (kN)	
	exp.	*comp.*	*exp.*	*comp.*	*exp.*	*comp.*	*exp.*	*comp.*
Nice 0.24*g*	0.72	0.61	65.9	65	200	200	202	190
S. Fr. 1.13*g*	1.2	1.1	106	90	280	240	271	270
Nice 0.40*g*	1.35	1.1	86.6	75	280	240	217	225
Nice 0.71*g*	4.4	3.9	111	120	345	380	312	310

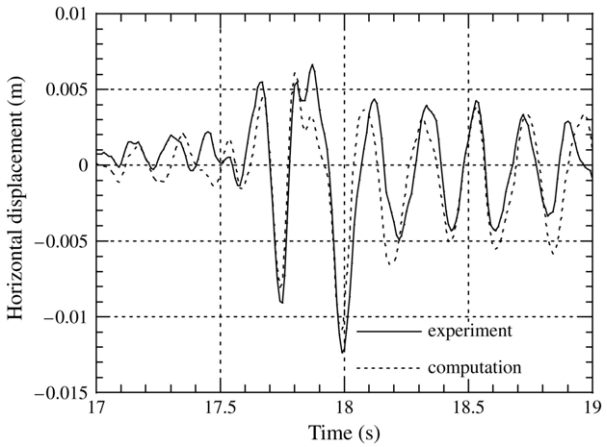

Fig. 8. CAMUS I – displacement time history at the top (San Francisco 1.13*g*).

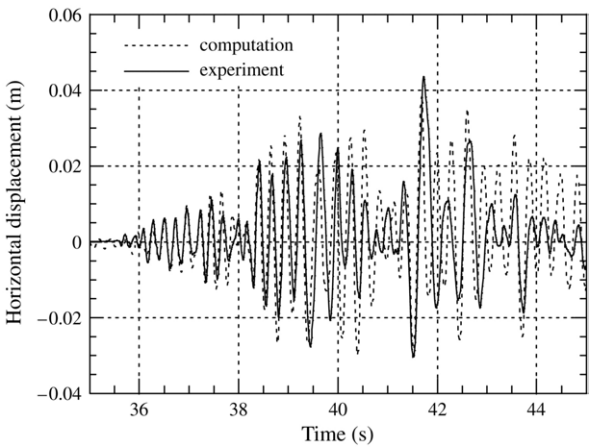

Fig. 9. CAMUS I – displacement time history at the top (Nice S1 0.71*g*).

satisfactorily the maximum displacement and there is no shifting between the curves (Fig. 10). The Melendy Ranch seismic input motion caused important damage to the mock-up with extensive cracking and beginning of crushing at the wall extremities. Permanent displacements were observed at the end of the sequence, sign of residual cracks and significant yielding of the reinforcement bars. A large crack appeared throughout the base of each wall. The bending moment reached the value of the ultimate moment ($M_{Rd} = 400$ kN m: design flexural capacity for the selected curtailment of vertical bars). It is recalled that the maximum accelerations of the Melendy Ranch signal are around the natural frequency of the specimen. Results of the simulation are compared with the experimental results in terms of displacements at the fifth floor and moments at the upper part of the footing and show a fairly good agreement (Figs. 11 and 12). Table 7 presents the comparison between model and experiment for the complete loading sequence. Results are satisfactory for the three first sequences. However, some differences appear later on the displacements. This is due to the fact that no calibration of the numerical model has taken place – the model is more rigid than the specimen. One has also to keep in mind the limitations of the approach (bond slip and buckling are not taken into account, the interaction with the shaking table is quite complex and changes with the evolution of damage, constant Rayleigh damping . . .).

Table 6
CAMUS III – modal analysis

	Predicted frequencies (Hz)	Measured frequencies (Hz)
1*st mode*	7.25	6.88
2*nd mode*	20.0	20.0

4.3. Variation of the axial force

Numerical and experimental results show a variation of the axial force at the base of both mock-ups. As the cracks close, shock is induced, stiffness changes suddenly and the second mode (pumping mode) is excited [38]. This variation of the vertical dynamic forces is important and for severe loading it can even double or cancel the axial force due to the dead weight of the specimen. Experimentally, the phenomenon can be quantified by the measurement of an induced vertical acceleration at the shaking table.

The numerical parameter that helps reproduce this coupling between flexural and axial bending is the crack closure function σ_f of Eq. (13). Computations are performed with different forms of the crack closure function for the CAMUS I specimen (Fig. 13). Results presented in Table 8 show that the local behaviour of concrete plays a very important role in the global structural response and that the crack closure function can be identified for the different levels of loading.

Fig. 14 presents a sequence of the variation of the moment and the dynamic variation of the axial force

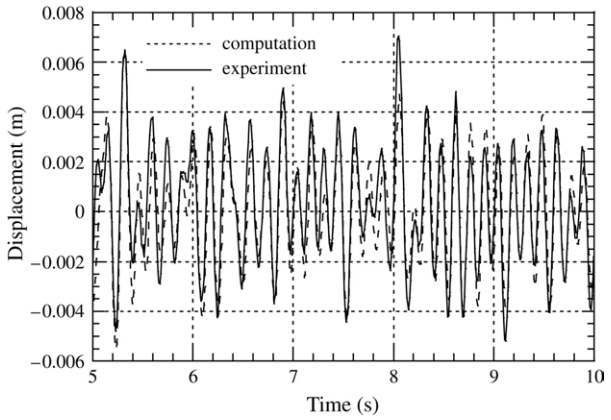

Fig. 10. CAMUS III – displacement time history at the fifth floor (Nice S1 0.42*g*).

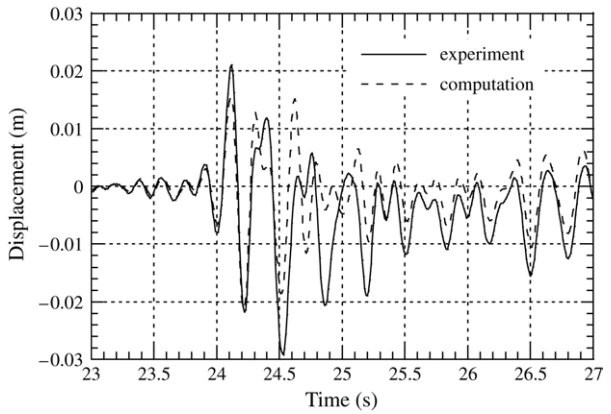

Fig. 11. CAMUS III – displacement time history at the fifth floor (Melendy Ranch 1.35*g*).

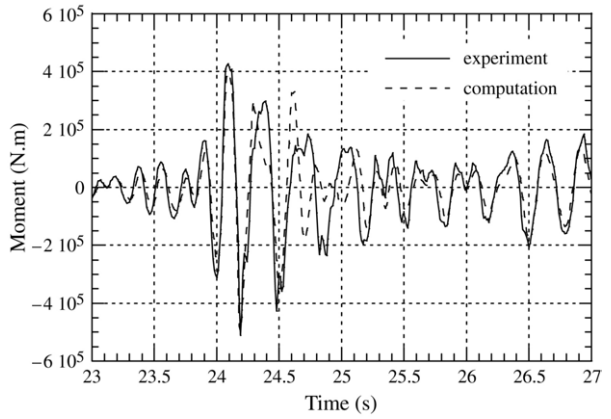

Fig. 12. CAMUS III – moment time history at the upper part of the footing (Melendy Ranch 1.35*g*).

– referred to a zero initial value – of the CAMUS III specimen (computation). During the closure of the cracks (displacement or moment equal to zero) a higher compression appears suddenly. A tension force of the same order of magnitude immediately follows this dynamic axial compression. For this calculation the crack closure function

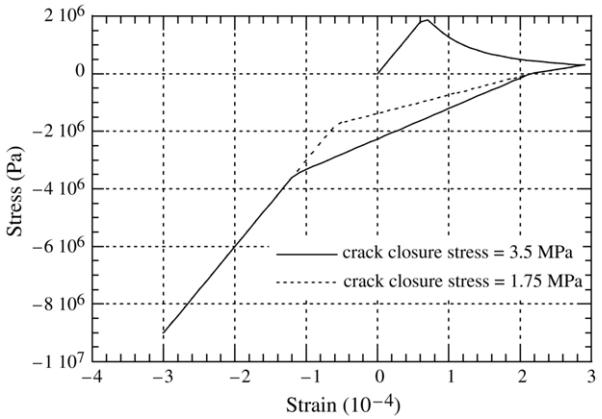

Fig. 13. Concrete model – effect of the crack closure stress on the slope of the stiffness recovery during cyclic loading.

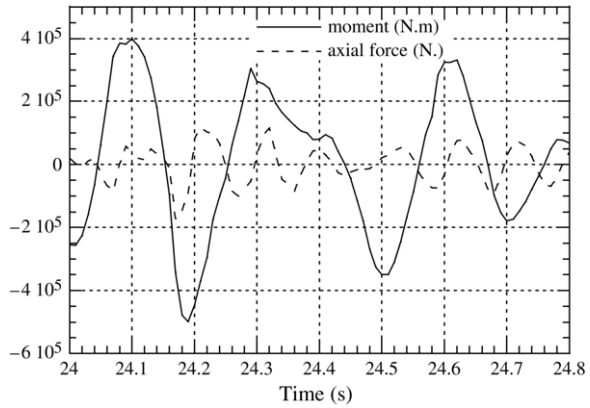

Fig. 14. CAMUS III – axial force and moment time history (computation).

σ_f is chosen equal to 1.3 MPa. If a weaker law crack closure function was chosen the stiffness change would have been more gradual and thus shocks would have been avoided and the extension–compression mode not excited [39].

4.4. Steel strain and damage distribution

The final crucial point in modelling pertains to computing the corresponding local level of degradation for both concrete and steel. Fig. 15 shows a typical result of this kind with the level of damage in concrete and the irreversible strains in steel at the end of the complete loading sequence for the CAMUS I specimen. One can see that the global trend observed experimentally is recovered in computations at this local level. The location of the critical region is positioned on the upper level. This particular behaviour is mainly due to the effect of the second pumping mode, whose primary effect results in shifting the failure region. Fig. 15 clearly demonstrates however that the computed strains always underestimate the experimentally obtained values.

After the Melendy Ranch seismic input motion, the strain gauges situated just above the level of the construction joint of the first floor of the CAMUS III specimen indicated high

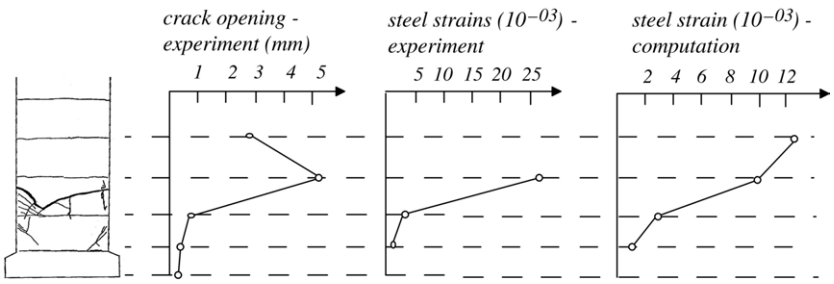

Fig. 15. CAMUS I – degradation of the specimen at the end of the analysis. Location of the cracks on the instrumented wall at the end of the loading sequence. Measured and computed strains (maximum values).

Fig. 16. CAMUS III – specimen at the end of the test (right wall).

strain values at this level on the one hand, and much lower values at the level corresponding to the second and third floor, on the other hand (see also Table 9). Consequently damage seemed to be concentrated at the level of first story with large plastic rotation at the base. This fact was confirmed by the inspection of the specimen after the failure test (Nice S1 – 1.0*g*): almost all the vertical steel reinforcement bars were broken and buckled just above the level of the first construction joint. The zone where rupture of the bars took place followed the main cracks at the base (Fig. 16).

The damage variables D_1 and D_2 (Eq. (12)) vary normally between 0 (non damaged section) and 1.0 (completely damaged section). By filtering their values between 0.95 and 1.0 we omit the micro-cracks and we have an image of the bigger cracks of the model. Fig. 17 presents the damage pattern due to compression and tension at the end of the calculation for the complete loading program. Comparison with the actual position of cracks shows that again the model is able to reproduce the global trend observed experimentally (creation of the plastic zones at the base of the walls this time). The wall is mainly damaged at the base and that is in accordance with the EC8 design philosophy ("monofuse" concept).

Table 9 presents the comparison between the measured and the computed steel strains at different locations at the end of the loading program. Although the model reproduced correctly these deformations for the points B and C, the results were not so satisfactory at point A where several steel bars were broken (Fig. 17 and Table 9). A constitutive model based on a continuum mechanics theory has difficulties in reproducing discrete phenomena as the local behaviour of materials at areas were significant cracks appear. Due to the small reinforcement ratio, the failure phenomenon can only happen by rupture of the steel bars under tension, thus post-peak behaviour cannot be well represented for both specimens. This is more obvious for the CAMUS I specimen where the model is able to reproduce qualitatively but not quantitatively the distribution of strains (see Fig. 15). Having less reinforcement, the CAMUS I specimen is more prone to localised deformations leading to rupture. The lack of information at the local scale (for example real strain in a steel bar at the location of a crack) is the major drawback preventing the designer from expressing physical criteria describing rupture.

5. Conclusions

The experimental campaigns of the CAMUS I and III specimens were an excellent opportunity to test the ability of the proposed numerical tools to simulate the non-linear behaviour of structures following different design philosophies. The CAMUS III design follows EC8 provisions that localize damage at the base of the wall and keep the upper stories linear ("monofuse" concept). CAMUS I is designed according to the French practice that opts for a "multifuse" design where damage is distributed throughout the height of the structure. This last approach leads to a multiplication of the dissipation zones, decreases the amount of steel needed and is interesting especially at areas with low to medium earthquake risk.

Both structures are simulated using Bernoulli multi-layered beam elements and advanced constitutive laws based on damage mechanics and plasticity. The advantage of using such beam elements is that engineers are familiar with them and that the resulting mesh has a relatively small number of degrees of freedom allowing for parametrical

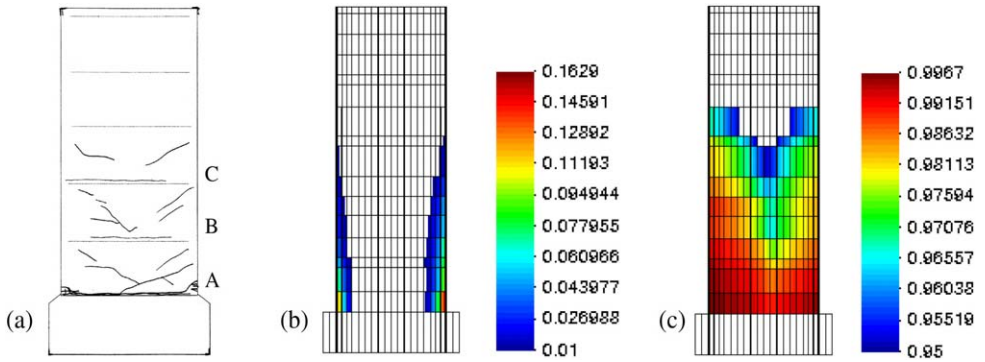

Fig. 17. CAMUS III – cracking of the wall at the end of the experiment (a) damage pattern due to compression (b) due to tension (c).

Table 7
CAMUS III – global response comparisons

	Disp. fifth fl. (cm)		Shear force (kN)		Moment (kN m)		Axial force (kN)	
	exp.	*comp.*	*exp.*	*comp.*	*exp.*	*comp.*	*exp.*	*comp.*
*Nice S*1 0.42*g*	0.7	0.6	79.6	78.8	263	247	222	232
*Nice S*1 0.24*g*	0.4	0.3	48.2	32.8	147	132	198	208
Mel. R 1.35*g*	2.9	2.1	151	153	510	469	374	348
*Nice S*1 0.64*g*	2.7	1.7	124	83.8	401	289	304	246
*Nice S*1 1.0*g*	4.7	2.4	140	123	410	364	314	292

Table 8
CAMUS I – vertical forces (kN): experimental and numerical results for various values of σ_f Eq. (13)

	$\sigma_f = 3.5$ MPa	$\sigma_f = 1.75$ MPa	$\sigma_f = 1.3$ MPa	$\sigma_f = 1.0$ MPa	Experiment
Nice S1 0.24*g*	115	119	**120**	120	**138**
San Francisco 1.13*g*	150	160	**200**	218	**198**
Nice S1 0.40*g*	119	132	**155**	165	**146**
Nice S1 0.71*g*	140	190	**240**	265	**248**

Table 9
CAMUS III – maximum plastic deformations of steel bars at the base at the end of the loading program

Def. steel	*Test* (%)	*Model* (%)
Point A	[a]	0.76
Point B	0.3	0.38
Point C	0.25	0.14

[a] Excessive plastic deformation or broken steel bar.

studies. Comparison with the experimental results proves the ability of the proposed strategy to reproduce the global but also the local behaviour of the specimens in terms of displacements, forces and damage distribution patterns. The different dissipation zones are also correctly reproduced even under severe loading.

The small differences appearing between the experimental and the numerical results for the CAMUS III specimen in terms of the displacements are due to the fact that no calibration of the model has been performed making this comparison similar to the one of a "blind test". One has also to consider the limitations of the approach (bond slip is not taken into account, linear shear, complexity of boundary conditions).

An interesting point of this study is the variation of the axial forces that the numerical and experimental results have demonstrated. This phenomenon has a major effect on the structural response as these types of walls have low vertical stresses due to gravity. Modelling correctly such a structural feature is important for R/C structures where the interaction between flexural bending and normal loading has to be taken into account. Results of the simulation depend primarily on the parameter of the local constitutive relation controlling the closing and opening of the cracks in the concrete during the loadings.

The major drawback of this approach is that a model based on continuum damage mechanics is inadequate to capture localized, discrete phenomena like excessive plastic deformations and significant cracks. In order to remain within the framework of simplified methods recent developments investigated the possibility to extend the method by introducing simple failure criteria and dissipation at a local (material) level in order to couple the state of cracking with the level of dissipation by frictional sliding

of the crack surfaces [40]. Another possibility is to use non-local approaches [41] or to couple the damage model with local second gradient models [42,43]. Work is in progress in that direction.

Acknowledgement

Part of this work was granted from the European program ICONS [37].

References

[1] AFNOR. Règles PS applicables aux bâtiments, dites Règles PS92. NF P 06-013 / DTU Règles PS92; 1995.

[2] EC8. ENV 1998-1-3, Eurocode 8, Design provisions for earthquake resistance of structures – Part 1–3: General Rules – Specific rules for various materials and elements, CEN; 1998.

[3] Owen DRJ, Hinton E. Finite elements in plasticity: theory and practice. Swansea (England): Pineridge Press Ltd; 1980.

[4] Ghavamian S, Mazars J. Stratégie de calculs simplifiés pour l'analyse du comportement des structures en BA: le code EFICOS. Revue Française de Génie Civil 1998;2(1):61–90.

[5] Guedes J, Pégon P, Pinto A. A fibre Timoshenko beam element in CASTEM 2000. Special publication Nr. I.94.31, J.R.C., I-21020, Ispra (Italy): Joint Research Center; 1994.

[6] Spacone E, Filippou FC, Taucer FF. Fiber beam–column model for nonlinear analysis of R/C frames. I: Formulation. Earthquake Engineering and Structural Dynamics 1996;25(7):711–25.

[7] Petrangeli M, Pinto PE, Ciampi V. Fiber element for cyclic bending and shear of RC structures. I: Theory. Journal of Engineering Mechanics 1999;125(9):994–1001.

[8] Kotronis P, Davenne L, Mazars J. Poutre 3D multifibre Timoshenko pour la modélisation des structures en béton armé soumises à des chargements sévères. Revue Française de Génie Civil 2004;8(2–3): 329–43.

[9] Kotronis P, Mazars J. Simplified modelling strategies to simulate the dynamic behaviour of R/C walls. Journal of Earthquake Engineering 2005;9(2):285–306.

[10] Chopra AK. Dynamics of structures: theory and applications to earthquake engineering. 2nd ed. Prentice-Hall; 2001.

[11] Newmark NM. A method of computation for structural dynamics. ASCE Journal of Engineering Mechanics Division 1959;85:67–94.

[12] Mazars J, Pijaudier-Cabot G. Continuum damage theory – application to concrete. ASCE Journal of Engineering Mechanics 1989;115: 345–65.

[13] Dubé JF. Modélisation multicouche des voiles en béton armé. Revue Française de Génie Civil 1997;1(2):285–307.

[14] Mazars J, Kotronis P, Davenne L. A new modelling strategy for the behaviour of shear walls under dynamic loading. Earthquake Engineering and Structural Dynamics 2002;31(4):937–54.

[15] Kotronis P, Mazars J, Davenne L. The equivalent reinforced concrete model for simulating the behavior of shear walls under dynamic loading. Journal of Engineering Fracture Mechanics 2003;7–8: 1085–97.

[16] Bathe KJ. Finite element procedures in engineering analysis. Englewood Cliffs (NJ): Prentice-Hall; 1982.

[17] Pégon P. Derivation of consistent proportional viscous damping matrices. Joint Research Center report, No I.96.49, Ispra, Italy, 1996.

[18] Ghavamian S. Méthode simplifiée pour la simulation du comportement sismique des structures en béton armé. Traitement des effets de l'élancement et estimateur d'erreurs. Ph.D., Ecole Normale Supérieure de Cachan; 1998.

[19] Lemaitre J, Chaboche JL. Mechanics of solids material. Cambridge University Press; 1990.

[20] Armstrong PJ, Frederick CO. A mathematical representation of the multiaxial Bauschinger effect. G.E.G.B. Report RD/B/N 731; 1966.

[21] Kracjinovic D, Fonseka GU. The continuous damage theories of brittle materials, Part I and II. ASME Journal of Applied Mechanics 1981;48:809–24.

[22] Willam KJ, Pramono E, Sture S. Fundamental issues of smeared crack models. In: Shah SP, Swartz SE, editors. Int. conf. on fracture of concrete and rock. SEM/RILEM; 1987. p. 142–3.

[23] Yazdani S, Schreyer L. Combined plasticity and damage Mechanics model for plain concrete. Journal of Engineering Mechanics 1990; 116(7):1435–51.

[24] Pijaudier-Cabot G. Continuum damage modelling. Constitutive Modelling of Geomaterials 2000;4(5):33–57.

[25] Fardis MN, Alibe B, Tassoulas JL. Monotonic and cyclic constitutive law for concrete. Journal of Engineering Mechanics 1983;1099(2): 516–36.

[26] Balan TA, Filippou FC, Popov EP. Constitutive model for 3D cyclic analysis of concrete structures. Journal of Engineering Mechanics 1997;123(2):143–53.

[27] Bazant ZP, Prat PC. Microplane model for brittle-plastic material: I. Theory. Journal of Engineering Mechanics 1988;14(10):1672–88.

[28] Fichant S, Pijaudier-Cabot G, La Borderie C. Continuum damage modelling: approximation of crack induced anisotropy. Mechanics Research Communications 1997;24:109–14.

[29] Fichant S, La Borderie C, Pijaudier-Cabot G. Isotropic and anisotropic descriptions of damage in concrete structures. International Journal of Mechanics of Cohesive-Frictional Materials 1999;4:339–59.

[30] La Borderie C. Phénomènes unilatéraux dans un matériau endommageable: modélisation et application à l'analyse de structures en béton. Ph.D., Université Paris VI; 1991.

[31] Queval JC, Combescure D, Sollogoub P, Coin A, Mazars J. CAMUS experimental program. In-plane tests of 1/3 scaled R/C bearing walls. In: Bisch P, Labbé P, Pecker A, editors. Proc. XIth European conference of earthquake engineering – 98, cd-rom. Paris: CNIT La Défense; 1998.

[32] Combescure D, Chaudat Th. ICONS European program seismic tests on R/C bearing walls. CAMUS III specimen. Rapport DMT, SEMT/EMSI/RT/00-014/A, CEA Saclay; 2000.

[33] 1st CAMUS Benchmark Organizing Group. CAMUS international benchmark, Report I, Specimen and loading characteristics. Specification for the participants report. SEMT/EMSI/RT/98-066A, CEA Saclay; 1998.

[34] 1st CAMUS Benchmark Organizing Group. CAMUS international benchmark, Report II, experimental results. Synthesis of the participant reports. SEMT/EMSI/RT/98-067A, CEA Saclay; 1998.

[35] CAMUS III Benchmark Organizing Group. CAMUS III international benchmark, synthesis of the participant reports. In: Post-FraMCoS-4 workshop 'seismic loading effects on structural walls'. 2001.

[36] CAMUS III Benchmark Organizing Group. CAMUS III international benchmark, Participant reports, Post-Tests calculations. In: Post-FraMCoS-4 workshop 'seismic loading effects on structural walls'. 2001.

[37] CAFEEL-ECOEST/ICONS Thematic report N.5. Shear walls structures. Reynouard JM, Fardis MN, editors, Severn RT, Bairrão R, general editors. LNEC, September, 2001.

[38] Ragueneau F, Mazars J. Damping and boundary conditions, two major points for the description of the seismic behaviour of R/C structures. In: Bisch P, Labbé P, Pecker A, editors. Proc. XIth European Conference of Earthquake Engineering – 98, cd-rom. Paris: CNIT La Défense; 1998.

[39] Lago A, Combescure D. Numerical analysis of CAMUS III using a fiber model. Nonlinear push over and dynamic analysis. Rapports DMT SEMT/EMSI/RT/ 98-054 A, CEA Saclay; 1998.

[40] Ragueneau F, La Borderie C, Mazars J. Damage model for concrete

like materials coupling cracking and friction, contribution towards structural damping: first uniaxial application. Mechanics Cohesive Frictional Materials 2000;5:607–25.
[41] Pijaudier-Cabot G, Bažant ZP. Nonlocal damage theory. Journal of Engineering Mechanics 1987;113:1512–33.
[42] Chambon R, Caillerie D, Matsushima T. Plastic continuum with microstructure, local second gradient theories for geomaterials: localization studies. International Journal of Solids and Structures 2001;38:8503–27.
[43] Kotronis P, Chambon R, Mazars J, Collin F. Local second gradient models and damage mechanics: application to concrete. Turin, Italy, 20–25 March. Org. ICF, cd paper no 5712; 2005.